Reusable and highly sensitive SERS immunoassay utilizing gold nanostars and a cellulose hydrogel-based platform

Maria João Oliveira[a,b,c], Inês Cunha[a], Miguel P. de Almeida[d], Tomás Calmeiro[a], Elvira Fortunato[a], Rodrigo Martins[a], Luís Pereira[a,e], Hugh J. Byrne[f], Eulália Pereira[d], Hugo Águas[a,*], and Ricardo Franco[b,c,*]

---

a. CENIMAT-i3N, Departamento de Ciência dos Materiais, Faculdade de Ciências e Tecnologia, FCT, Universidade Nova de Lisboa, 2829-516 Caparica, Portugal; i.cunha@campus.fct.unl.pt (I.C); t.calmeiro@campus.fct.unl.pt (T.R.C.); emf@fct.unl.pt (E.F.); rfpm@fct.unl.pt (R.M.)

b. Associate Laboratory i4HB, Institute for Health and Bioeconomy, Faculdade de Ciências e Tecnologia, Universidade NOVA de Lisboa, 2829-516 Caparica, Portugal; mj.oliveira@campus.fct.unl.pt (M.J.O.)

c. UCIBIO, REQUIMTE, Departamento de Química, Faculdade de Ciências e Tecnologia, Universidade NOVA de Lisboa, 2829-516 Caparica, Portugal

d. REQUIMTE/LAQV, Departamento de Química e Bioquímica, Faculdade de Ciências da Universidade do Porto, 4169-007 Porto, Portugal; mpda@fc.up.pt (M.P. de A.); eulalia.pereira@fc.up.pt (E.P.)

e. AlmaScience, Campus da Caparica, 2829-516 Caparica (Portugal)(lmnp@fct.unl.pt (L.P.)

f. FOCAS Research Institute, Technological University Dublin, Camden Street, Dublin 8, Ireland. Hugh.Byrne@tudublin.ie (H.J.B.)

* Correspondence: hma@fct.unl.pt (H.A.); ricardo.franco@fct.unl.pt (R.F.)

1

Contents

1. Synthesis and characterization of gold nanostars

AuNPs and AuNSs were synthesised and characterised as previously reported, since the method proved to have a good batch-to-batch reproducibility[1]. AuNPs with a diameter of 12 nm (λ_{LSPR} = 519 nm) were synthesised by the method reported by Ojea-Jiminéz et al.[2], and then used as seeds to obtain the AuNSs. As shown in Figure S1, the size, morphology, and concentration of AuNSs were confirmed using UV-Vis and SEM. As the SEM micrograph shows, AuNSs are characterised by a central core with multiple spikes and the average tip-to-tip length observed was ≈70 nm. The typical broad localised surface plasmon resonance (LSPR) band around 700 nm results from the high anisotropy of the AuNSs, giving rise to multiple plasmonic modes[3,4]. UV-Vis spectra were used to determine the AuNSs molar concentration (ca. 0.7 nM)[5].
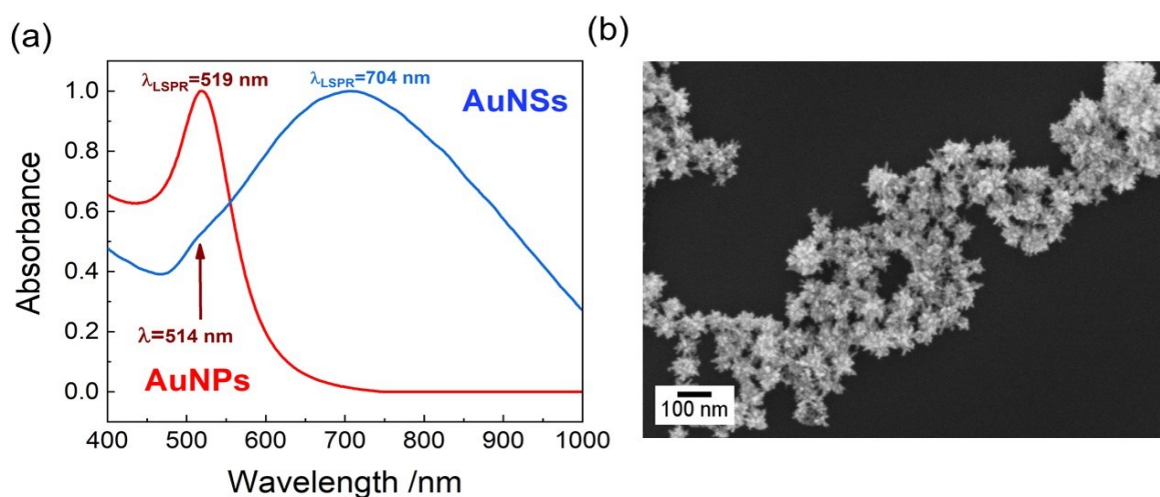

Figure S 1 - (a) UV-Vis spectra of AuNPs (red line) and AuNSs (blue line). AuNPs synthesised by the method reported by Ojea-Jiminéz[2] allowed a diameter of 12 nm (λLSPR = 519 nm). These AuNPs were used as seeds to produce the AuNSs. The AuNSs present a LSPR band centred approximately at 704 nm and a large broadening due to their multiple resonances caused by the tips and edges. The small broad resonance at ≈514 nm is associated to transverse resonance within the branches or to plasmonic resonances of spherical protuberances[3,5]. (b) SEM micrograph of AuNSs after synthesis where it is possible to observe their characteristic anisotropic morphology.

2. Functionalisation of gold nanostars with MBA or DTNB

UV-Vis spectroscopy and agarose gel electrophoresis (AGE) were used to verify the functionalisation process i.e. the presence of MBA or DTNB after its addition to the AuNSs at a ratio of 1:50,000, as previously optimized)[1] (Figure S2). Considering the UV-Vis spectra, a 22 nm or 18 nm red-shift of the LSPR is observed for MBA or DTNB, respectively. This phenomenon occurs due to an increase in the local refractive index at the AuNS surface[6]. Since AuNSs are anisotropic, they show a large change in the refractive index due to the presence of "hot spots" (especially at tips or edges) responsible for enhanced electromagnetic fields[6–8]. Regarding AGE, two distinct behaviours are observed. As synthesized, non-functionalized AuNSs did not migrate in AGE, probably due to the loss of the weakly bound citrate ions or the presence of specific interactions between the gel and the nanoparticles[9]. Conversely, functionalized AuNSs present an electrophoretic mobility, corresponding to a full layer of MBA or DTNB covering the AuNSs[1] (Figure S2).
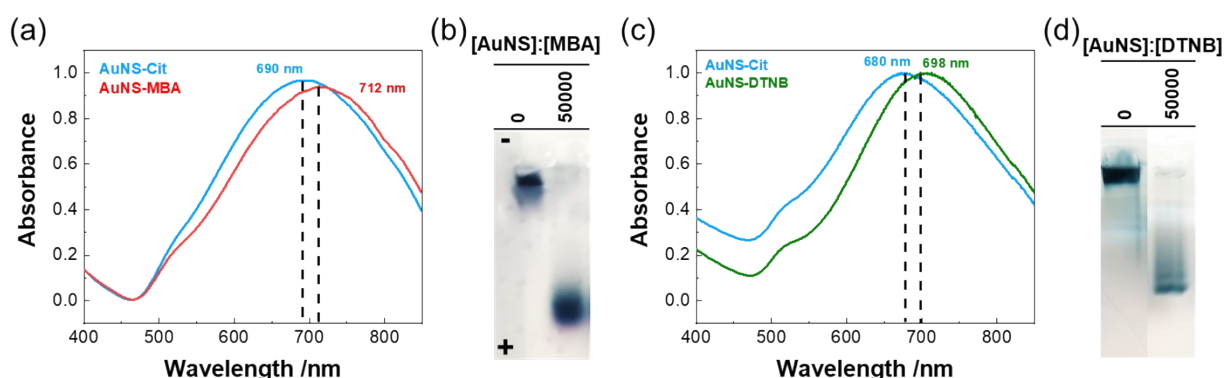

Figure S 2 - (a) UV-Vis spectra of non-functionalised AuNSs *i.e.* with citrate ions from the synthesis (blue line) and MBA-functionalised AuNSs (red line). The AuNSs present a LSPR band centred approximately at 690 nm and a large broadening due to their multiple resonances caused by the tips and edges. This LSPR is red-shifted to 712 nm when MBA is added to replace the citrate ions due to its thiol group which has a higher affinity for gold. (b) Photograph of an agarose gel where a difference in electrophoretic mobility can be readily distinguish MBA-functionalised AuNSs (second well) from the non-functionalised AuNSs (first well). (c) UV-Vis spectra of non-functionalised AuNSs *i.e.* with citrate ions from the synthesis (blue line) and DTNB-functionalised AuNSs (green line). The AuNSs present a LSPR band centred approximately at 680 nm and a large broadening due to their multiple resonances caused by the tips and edges. This LSPR is red-shifted to 698 nm when DTNB is added to replace the citrate ions due to its thiol group which has a higher affinity for gold. (d) Photograph of an agarose gel where a difference in electrophoretic mobility can be readily distinguish DTNB-functionalised AuNSs (second lane) from the non-functionalised AuNSs (first lane).

3. Covalent functionalisation with antibodies

AGE has been instrumental in determining the most suitable conditions to establish active and stable SERS-immunotags[1,10–14]. Therefore, the sandwich SERS-based immunoassay was simulated in AGE, by which the electrophoretic mobilities of the different stages in the bioconjugation process were measured. A horizontal agarose gel system was used in all experiments under a constant voltage of 150 V (E = 10 V/cm) in a mini-sub cell GT (Bio-Rad, Portugal) with agarose; 0.3% in Tris-acetate-EDTA (TAE) buffer 0.125×. Samples for AGE, were centrifuged at 9500 g at 10 °C for 10 min, and the supernatant was discarded. Fifteen µL of potassium phosphate buffer (pH = 7.4, 5 mM) were used to resuspend the pellet and samples were loaded in the gel. Digital pictures of the gels were processed by eReuss software (freely available at https://github.com/lkrippahl/eReuss), providing an accurate measurement of the red bands migration in agarose, and thus allowing calculation of electrophoretic mobility.

Electrophoretic mobility (µ) is defined as the observed rate of migration of a component (ν) divided by the electric field strength (E) in a given medium[1]. In the case of AGE, a solid support medium, only apparent values can be determined. AGE mobilities are represented as variations relative to the maximum mobility band (Δµ).

As for anti-HRP binding to AuNS-MBA by physisorption interactions[1], covalent conjugation also leads to a lower migration of SERS-immunotags toward the positive pole. As shown in Figure S 3, the electrophoretic mobility of SERS-immunotags was lower for covalent conjugation (red triangles) than for the physisorption-based conjugation (blue circles), in all conditions tested. In physisorption conjugation, the decrease in electrophoretic mobility is related to a higher number of antibodies adsorbed to the AuNSs surface, thus increasing the hydrodynamic size and partially cancelling the global net charge[15]. Herein, the amount of anti-HRP used corresponded to the full antibody corona around the AuNSs by physisorption adsorption[1]. Thus, differences in electrophoretic mobility between the physisorption and the covalent SERS-immunotags are determined by the coupling efficiency; as more antibody bound to the AuNSs translates into a decrease of electrophoretic mobility[14]. Hence, it is plausible to assume that the crosslinking reaction allowed a higher amount of the anti-HRP molecules to be attached to the AuNS-MBA. All electrophoretic mobilities were subjected to one-way ANOVA with Tukey's multiple comparison test for the means. Only when the means between physisorption and covalent bioconjugations were significantly different, the covalent bioconjugation was considered successful.

Several different experimental parameters were optimized, namely:

pH - MES buffer is a non-coordinating buffer and was chosen as it is known as one of the most effective for coupling reaction[13,16,17]. In Figure S 3A, from all the tested pH, the antibody was mostly coupled to AuNSs at pH 6.5. At pH 7, the coupling reaction is less effective since the pH of the reaction is more alkaline than that recommended for EDC activation reaction[18]. As a result, the amount of antibody conjugated with AuNSs is lower (as seen by the higher value of electrophoretic mobility in Figure S 3A). However, at pH 6, the diminished colour of the migration band observed reflects the aggregation of AuNSs during the coupling reaction.

Time - The effect of incubation time on the coupling efficiency was evaluated for 1, 7.5, 15 and 30 minutes. The amount of antibody bound to the AuNSs increased for longer incubation time, as demonstrated by the lower electrophoretic mobility (Figure S 3B). Since the reactions for 30 and 15 minutes showed similar efficiencies, the 15 min was chosen for further assays as it ensures a quicker, yet efficient process.

[EDC]/[SNHS] - The EDC to SNHS molar ratio, is mentioned in several works, although very few report a systematic investigation to maximise the coupling efficiency[14,19–21]. The molar ratios of EDC to SNHS varied from 1:0 to 1:10. As verified in Figure S 3C, for the molar ratios 1:0 and 1:0.5, the coupling reaction resulted in lower coupling efficiency, thus highlighting the importance of using SNHS to stabilise the active intermediate with carboxylates. Increasing the molar ratio led to the same range of electrophoretic mobilities. There was a small decrease in conjugation yield with an excess amount of SNHS, since the migration bands showed a higher aggregation level (1:6 and 1:10 molar ratios). Excess SNHS might lead to the competition with the protein by the carboxyl groups activated with EDC[21]. For this reason, the ratio of EDC:SNHS chosen was 1:2 since it showed a higher significantly difference with no signs of aggregation.

The final crucial parameter evaluated was the concentration of EDC necessary for the coupling reaction (Figure S 3D). A series of EDC concentrations ranging from 0.005 to 100 mM were tested while the [EDC]/[SNHS] ratio was fixed at 1:2. It is evident from the lower electrophoretic mobility, that the most effective coupling conditions are observed for EDC concentrations of 10 and 50 mM. Low amounts of EDC showed a higher variance (p-value >0.05) which might be due to several populations of SERS-immunotags with distinct loads of antibody that results in different hydrodynamic sizes and electric charges. Also, lower coupling efficiency was observed at higher

concentrations of EDC, possibly due to a competitive process between the highly concentrated antibody, thus reducing the available quantity to react to the nanoparticle surface[14].

Optimised bioconjugation parameters for covalent conjugation, as evaluated by AGE, were MES buffer at pH 6.5, for a duration of 15 min and with a molar ratio of EDC:SNHS of 1:2 at an EDC concentration of 10 mM.
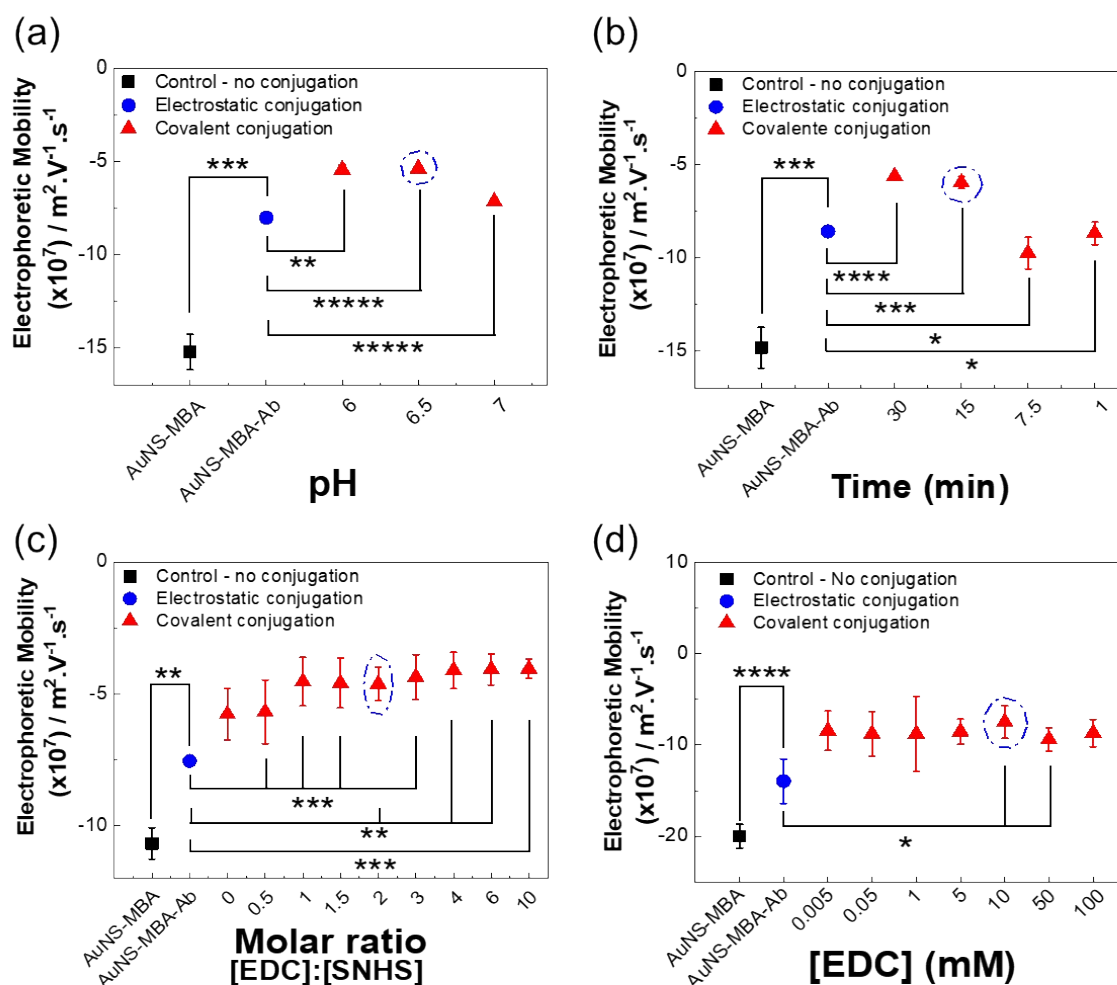

Figure S 3 - Covalent bioconjugation efficiency evaluation by AGE migration profiles. Optimisation of covalent bioconjugation was achieved by varying several parameters including (a) pH, (b) duration of the coupling reaction, (c) molar ratio between EDC:SNHS, and (d) concentration of EDC. Error bars correspond to standard deviation from three independent experiments (different sets of SERS-immunotags). One-way analysis of variance (ANOVA) followed by the Tukey's multiple comparison test were applied for statistical comparisons. *p≤0.05, **p≤0.01, ***p≤0.005, ****p≤0.001, ***** p≤0.0001 vs. physisorption conjugation.

4. Characterisation of SERS-immunotags and proof-of-concept for the biosensor

To test the functionality of the SERS-immunotags, colloidal suspensions were incubated with the respective antigen for the chosen antibody (HRP), followed by free anti-HRP antibody, simulating a positive assay result. Each stage of the bioconjugation formation and immunoassay simulation was monitored by UV-Vis spectroscopy, DLS and ζ-Potential. The adsorption of macromolecules on the AuNS-MBA surface causes a red-shift of the plasmon resonance band (Figure S 4)[1]. As mentioned before, the LSPR wavelengths shifts are a consequence of the changes in the refractive index of medium surrounding the nanostructures[22]. The slight broadening of the LSRP band can be a result of AuNSs aggregation or the higher degree of heterogeneity of AuNSs with different loads of proteins.
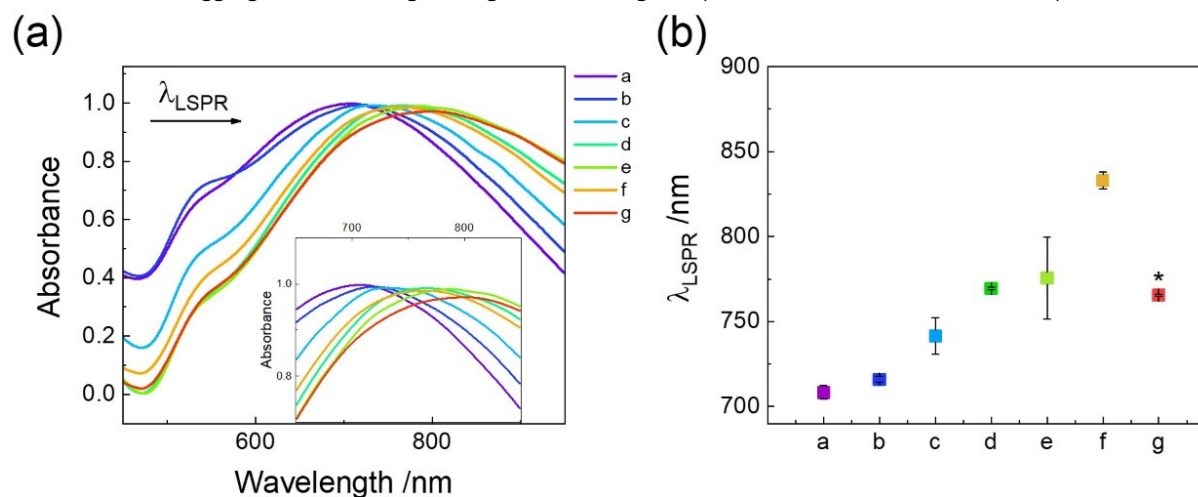

Figure S 4 - (a) UV-Vis spectra and (b) LSPR maximum of bioconjugation process by covalent coupling. Normalised optical spectra of as-synthesized nanostars (AuNS; a), with functionalisation (AuNS-MBA; b), after antibody conjugation (AuNS-MBA-anti-HRP; c) and blocking with BSA (SERS-immunotag; d). Followed the SERS-immunotag production, HRP was added to form (SERS-immunotag-HRP; e) and the sandwich immunoconjugate was completed with the antibody (SERS-immunotag-HRP-anti-HRP; f). The negative result for the assay was obtained with the addition of anti-HRP to the SERS-immunotags without HRP (SERS-immunotag-anti-HRP; g). Error bars correspond to the standard deviation from three independent experiments.

DLS and ζ-potential measurements of the SERS-immunotags were also obtained to further characterize SERS-immunotags formation (Table S 1 and Figure S 5). An average hydrodynamic diameter of 67.9±0.4 nm was observed for AuNS-MBA alone. The hydrodynamic diameter of the SERS-immunotags can be related to the amount of protein bound to the AuNSs since the diameter increases by each step of the conjugation. The subsequent additions of antibody, antigen, and antibody resulted in shifts of the average hydrodynamic diameter. In the covalent conjugation, the size increases from 67.9±0.4 nm to 149.1 ± 1.7 nm when the SERS-immunotag is formed. Compared to the physisorption bioconjugation approach, the hydrodynamic diameter of SERS-immunotags is ≈67 nm higher when the EDC-NHS is used to promote the covalent bond[1]. We suggest that the crosslinking event allows to attach more antibodies to the AuNSs surface or even to promote bounds such as nanoparticle-antibody-antibody. The dimensions of HRP are small, compared to SERS-immunotags (3.0 × 6.5 × 7.5 nm)[23], so there is no appreciable hydrodynamic size increase when the SERS-immunotags are incubated with HRP to form SERS-immunotags-HRP. The PDI values after each step of conjugation confirmed the results observed in UV-Vis spectroscopy.

Table S 1. DLS and Zeta potentials of SERS-immunotags and following steps toward sandwich immunoassay.

	Diameter (nm)	ζ-Potential (mV)	PDI
AuNS-MBA	67.9 ± 0.4	-31.6 ± 0.8	0.223
SERS-immunotags	149.1 ± 1.7	-25.6 ± 1.1	0.355
SERS-immunotags – HRP	149.0 ± 3.2	-22.1 ± 0.8	0.367
SERS-immunotags – HRP – anti-HRP	161.0 ± 1.3	-19.3 ± 0.9	0.368

Furthermore, ζ-potential can also be used for evaluating the nanoenvironment, being an indicator of the colloidal suspension stability. This value shows that the colloidal particles are electrically stabilised and hence can be used in the following assays for determining the positive detection of peroxidase by enzymatic assay and SERS activity. At pH 7, the AuNSs are negatively charged due to physiosorbed citrate ions (Table S 1 and Figure S 5). The global negative charge will interact with the positive charged residues of anti-HRP, consequently the zeta potential increases from -32 mV to -25 mV, consistent with adsorption of antibody on AuNSs surfaces. The following steps of HRP and further anti-HRP addition revealed small decreases in zeta potential to -22 mv and -19 mV, respectively, confirming successful adsorptions.
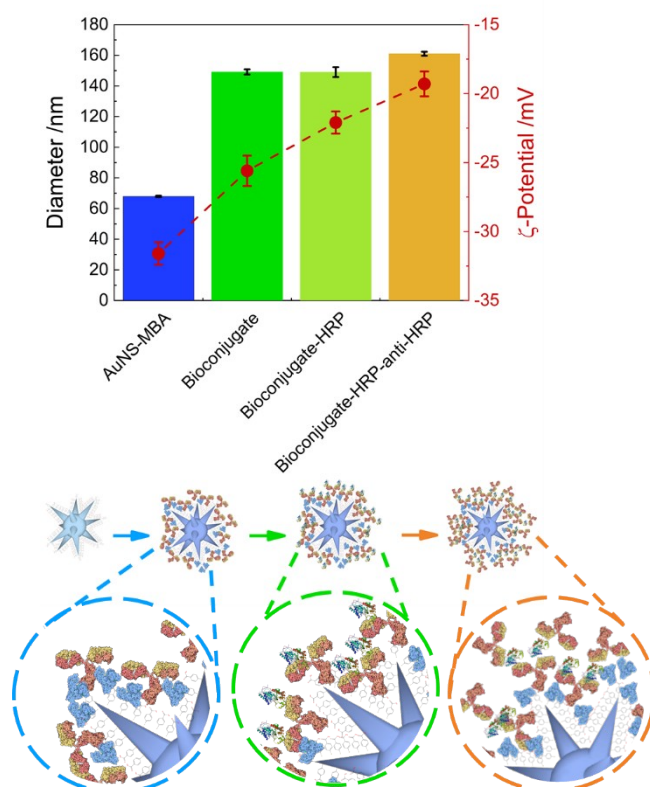

Figure S 5 - Hydrodynamic diameter and zeta-potential for several steps of SERS-immunotag formation (error bars are measurements of n = 3 ± standard deviation).

The functionality of the Anti-HRP AuNS-bound antibodies can be evaluated by peroxidase activity of the bound HRP antigens. Samples with no addition of HRP showed no enzymatic activity. On the other hand, an increase in the concentration of antibody leads to a higher amount of HRP captured by the antibodies present in the bioconjugates (Figure S6).
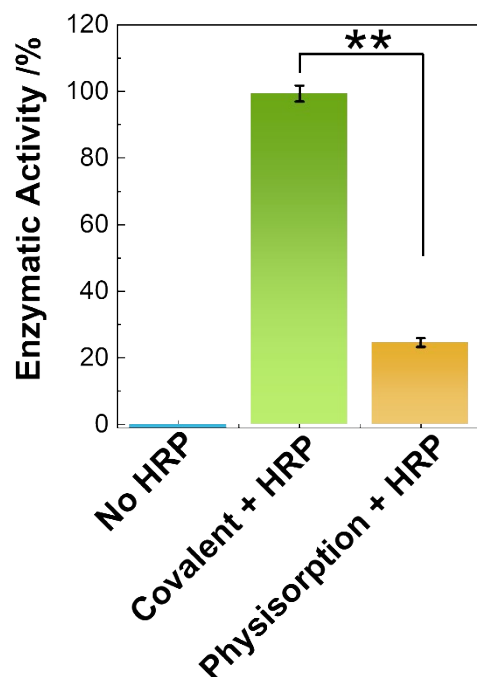
Figure S 6 - Functionality of the SERS-immunotags obtained by physiosorption (yellow bar) or covalent (green bar) methods, as evaluated by percent enzyme activity of bound HRP relative to total HRP in solution, before binding to the SERS-immunotags. The enzymatic activities for SERS-immunotags with HRP (green and yellow bars) and without HRP (blue bar) confirmed positive recognition by the AuNS-immobilised anti-HRP antibodies.

In Figure S7, the positive assay result, SERS-immunotag (with anti-HRP)/HRP/anti-HRP, is represented by a green bar, whereas the red bar corresponds to the negative result. The electrophoretic mobility from the negative result is analogous to the SERS-immunotag alone, since the anti-HRP antibodies added to the SERS-immunotags did not have the antigen to form the sandwich complex.
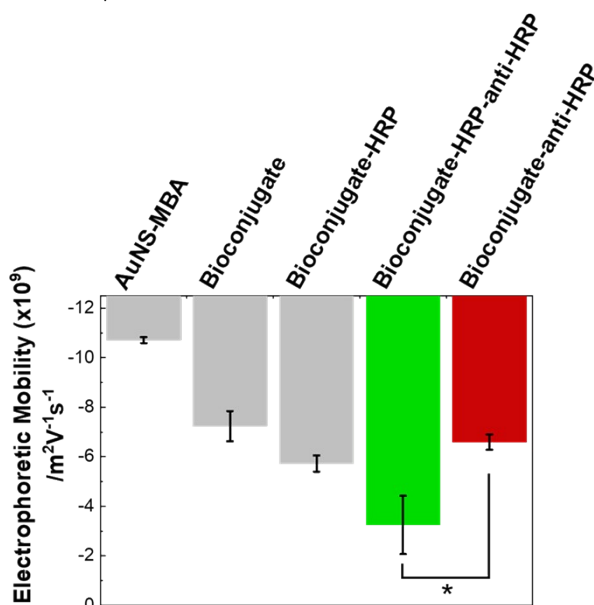

Figure S 7 - Proof-of-principle of the SERS-based immunoassay. Electrophoretic mobility was determined by AGE. The green bar corresponds to the sandwich complex formed during HRP antigen detection (positive result). The red bar corresponds to the negative result when no HRP antigen is present. Error bars correspond to the standard deviation from five independent experiments (different sets of SERS-immunotags). One-way analysis of variance (ANOVA) was applied for statistical comparison followed by the Tukey's multiple comparison test, $*p \leq 0.05$.

5. Characterisation of the regenerated cellulose hydrogel

As can be seen in Figure S 8, the phase difference did not change significantly after the TEMPO treatment on the cellulose. In the work of Orelma et al. an increase in phase difference was observed followed by an increase in surface roughness, which was attributed to a higher hydrophilic nature due to the increased water molecules bounded to the carboxylated cellulose[24]. However, the RCH and TO-RCH samples were immersed in PBS buffer during AFM analysis which might eliminate this effect.
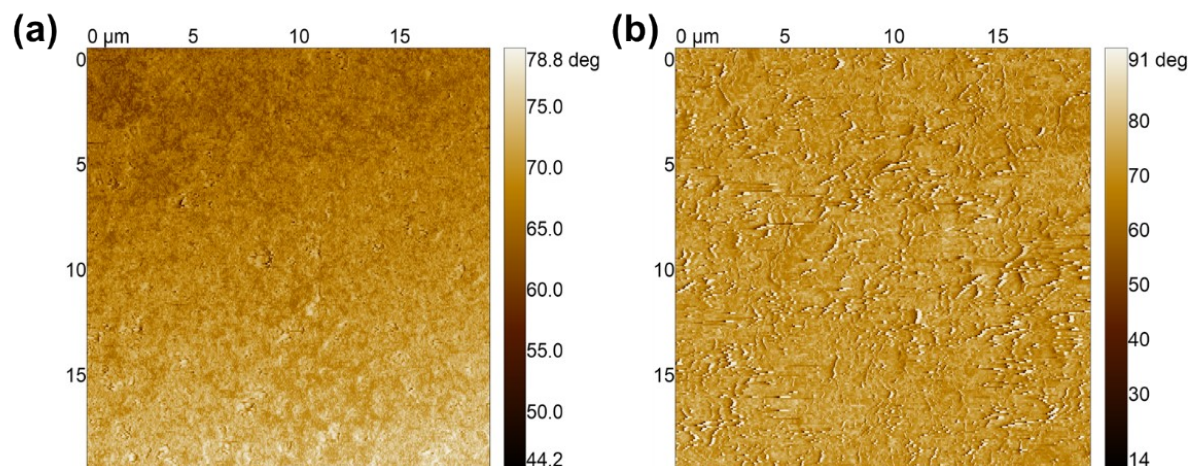

Figure S 8 - AFM images of the (a) unmodified RCH and (b)TEMPO-oxidated RCH.

FTIR spectroscopy was performed with a Thermo Nicolet 6700 Spectrometer (Waltham, MA, USA) equipped with a single bounce diamond crystal Attenuated Total Reflectance (ATR) sampling accessory (Smart iTR). Spectra were acquired with a 4 cm^{-1} resolution in the range of 4000–525 cm^{-1} with a 45° incident angle.
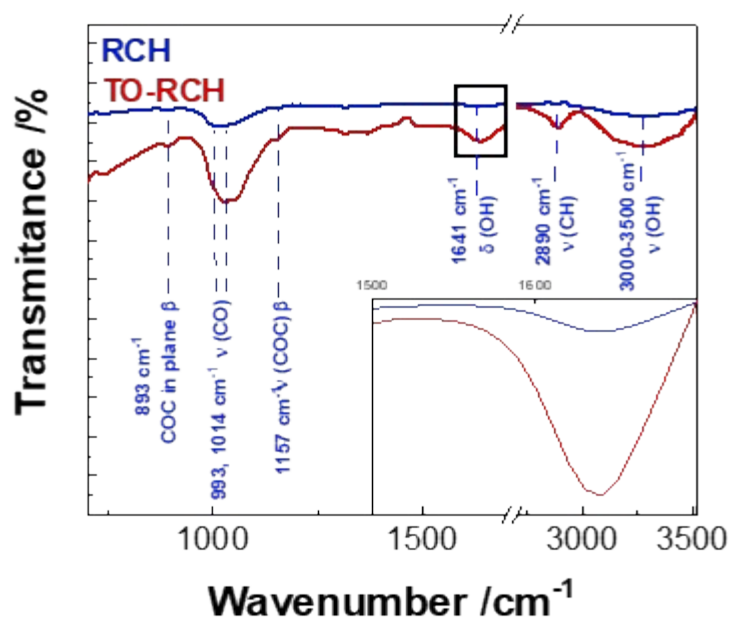

Figure S 9 - FTIR spectrum of the as-prepared (RCH, blue) and after activation by TEMPO (TO-RCH, red), with band assignments for the typical bands of cellulose[25]. The inset is a magnification of the 1500-1700 cm^{-1} region, evidencing the appearance of carboxyl-group broad bands, after TEMPO oxidation.

6. Classical least squares model

Multivariate curve resolution (MCR) methods are used for demultiplex the mixed spectrum into the different chemically meaningful components and provide a way to quantify the contribution of each component on the original mixed spectrum. The mixed Raman spectrum is assumed as a linear combination of the spectra of several pure components and the MCR methods aim to minimise the Euclidean distance between the pure components and an estimate of the transpose of coefficients from the corresponding components quantifying the contribution[26].

In a classical least squares model, we assume that the raw data is a product of a weighted sum of reference component spectra,

$$D = KC + E \tag{1}$$

Where D is the measure spectrum, K is a vector of the Raman spectrum of pure components and C is the vector of coefficients which quantify the contribution of each corresponding component in K. In other words, C is the coefficient values vector which dictates "how much" each basis vector contributes to each pixel from the measured signal, D. Because the measured spectrum and the pure substances spectra contain noise, the residuals are expressed by E, and represent the experimental error or remaining background. Usually, E is considered as noise and normally distributed[26].

Being a least square model means that we want to minimize the error in the reproduction of values of D over all wavenumbers, so from equation (1), we obtain:

$$E = D - KC \tag{2}$$

Applying the Euclidean norm of ε, i.e. $\|\varepsilon\|_2^2 = x^T x$, we get:

$$\|D - KC\|_2^2 = (D - KC)^T(D - KC) = C^T K^T KC - 2D^T KC + D^T D$$

To find the minimum of the function, we derive, $\nabla_x(x^T M x) = 2Mx$, and set equal to zero to find the contribution coefficients[26]:

$$\nabla_c(C^T K^T KC - 2D^T KC + D^T D) = 2K^T KC - 2K^T D = 0 \Leftrightarrow K^T KC = K^T D \Leftrightarrow$$
$$\Leftrightarrow C = (K^T K)^{-1} K^T D \tag{3}$$

The CLS analysis was then carried out with in-house scripts written in Python 3.8. The CLS analysis method assumes each point in the raw spectral map to be a mixture of reference component spectra. In other words, the raw spectrum is considered as a weighted sum of the linear contributions of the reference components, and the (supervised) CLS fitting process generates scores to represent the weightings of each constituent contribution[27]. The reference components were the pure Raman spectra of MBA and DTNB SERS-immunotags and the functionalised RCH.

7. Threshold value for application of the CLS method

The CLS method was applied to resolve complex SERS spectra. The corresponding coefficients of the MBA Raman probe from the SERS-immunotags and from the RCH from all the pixels were plotted, thus constructing the sandwich complex image. Admitting that the SERS signal of MBA is obtained from a positive detection of HRP bound to anti-HRP immobilised on the RCH platform, the number of events i.e. pixels, can be correlated with the concentration of HRP. Nevertheless, it is important to threshold the immuno-platform data in order to distinguish the immunocomplex from the capture platform and to avoid a high degree of error for the components tested and loss of information from the dataset [28]. Thus, |SERS maps of controls that explore the non-specific binding of SERS-immunotag to the capture platform, were performed and the component coefficient values were determined. From all coefficient values obtained, 95% were at or below 0.352, and consequently were deemed not to be positive immunocomplexes (Figure S 10)[28].
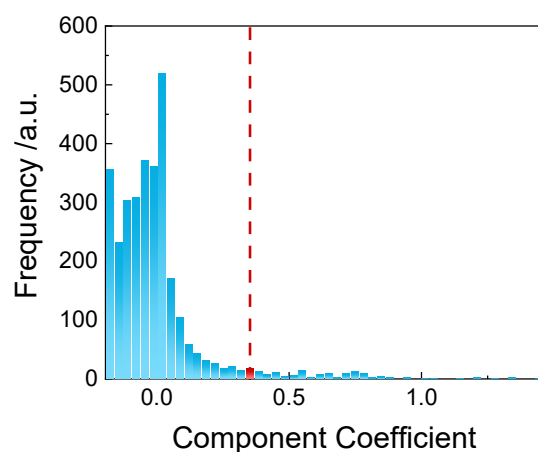

Figure S 10 - Histogram of component coefficient frequencies for blanks in the SERS immunoassay. The red dashed line represents the 0.352 component coefficient that was considered as the threshold for the positive detection of a SERS immunoassay.

8. Selectivity of the immunoassay

The selectivity of the SERS-based RCH immunoassay was assessed by testing the responses to a purified irrelevant antigen, namely *P. falciparum* His-Rich Protein 2 (*Pf*HRP2), used for malaria infection detection *vs.* positive detection using the target antigen, HRP. Figure S11 presents five randomly chosen spectra from the negative control *i.e.* with *Pf*HRP2 and five also randomly chosen from the positive assay *i.e.* with HRP.
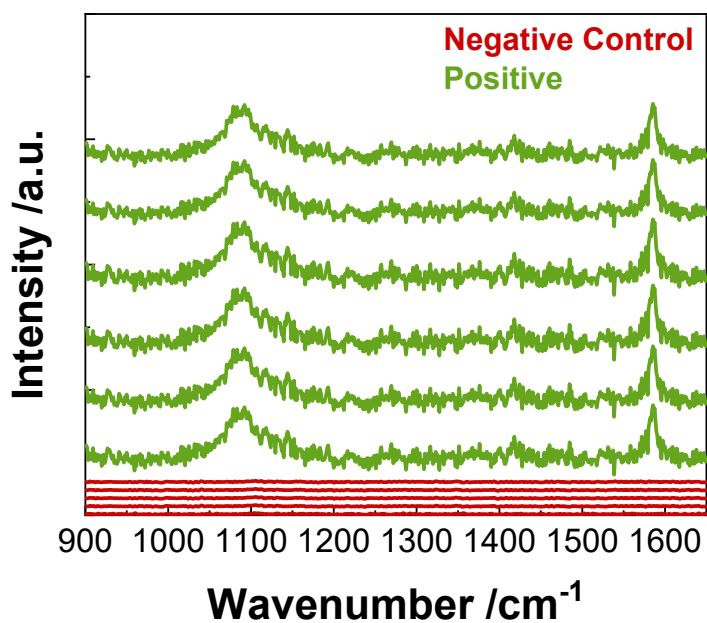

Figure S 11 - Selectivity response of the immunoassay. Five randomly chosen SERS spectra from the "Negative control" (red data) *i.e.* with *Pf*HRP2 and five randomly chosen SERS spectra from the "Positive" (green data) for the target antigen, HRP.

10. Reproducibility and stability examination.

The inter and intra-reproducibility of the SERS-based RCH immunoassay was studied by testing three independent batches of membrane functionalised with anti-HRP. Similar responses were obtained between different batches and within each batch with a relative standard deviation for the SERS signal of 13%, indicating a high reproducibility for all the four performed tests for each sample (time = 0 h in Figure S12A).

The activity of the immunoassay is dependent on the stability of SERS-immunotags, and of the antibodies immobilised on the membrane. Therefore, their activities were monitored independently by their enzymatic activity and by the SERS immunoassay after one week (168 h) (Figure S 12). The HRP bounded to the antibody attached to the membrane showed very good stability with a decreasing in activity only to 83%, after 168 h. After the same period, the SERS-immunotags showed 52% of their original activity, as well as a diminished capacity for immuno-detection, as evaluated by SERS, 87% (Figure S 12).
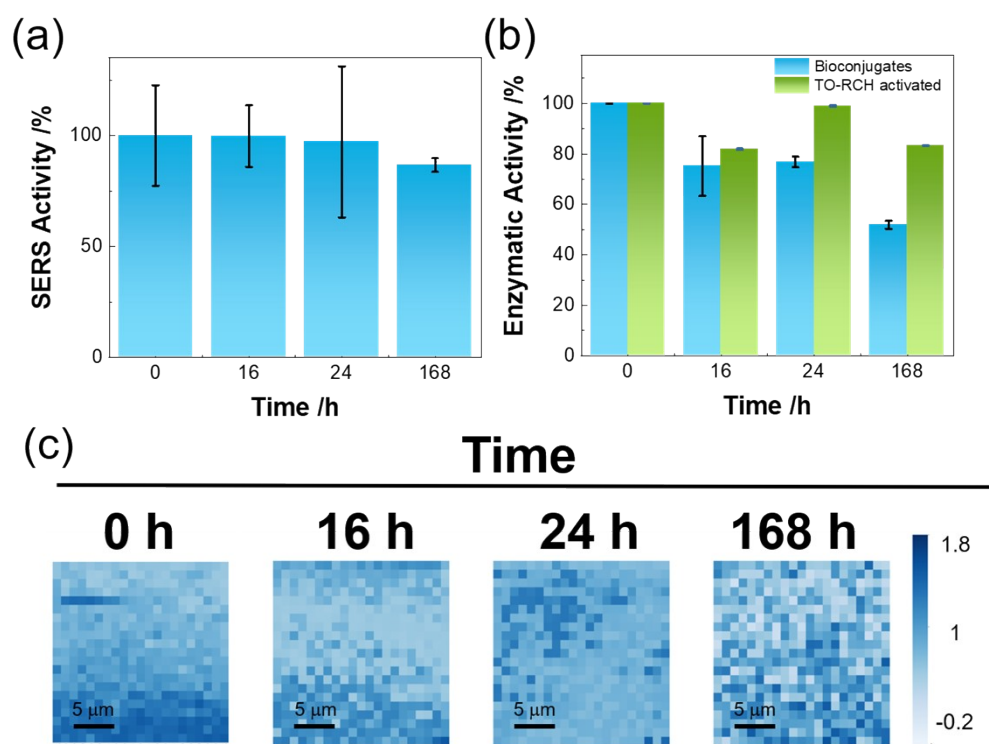

Figure S 12 - Time stability study. (a) Sandwich immunoassay SERS results for three independent batches of the capture platforms and MBA-SERS-immunotags. (b) Enzymatic activity for 0 h, 16 h, 24 h and after 168 h, for SERS-immunotags (blue bars) and the capture platform (green bars). Error bars correspond to the standard deviation from three independent experiments. (c) Four, randomly selected, pixelated SERS maps from the HRP stability study presented in (a).

11. Capture platform reusability

Biosensor regeneration was done by removing the SERS-immunotags and the target analyte, HRP, from the capture platform with 0.2 M glycine-HCl, and then washing with PBS to restore the capture platform for another analytical cycle with HRP. Figure S 13 shows SERS activity along seven analytical cycles with a regeneration step between each cycle. Figure S 14 shows the SERS activity as well as the enzymatic activity for the entire process of regeneration including the decrease in SERS and enzymatic activity when the capture platform is cleaned from the HRP and SERS-immunotags.
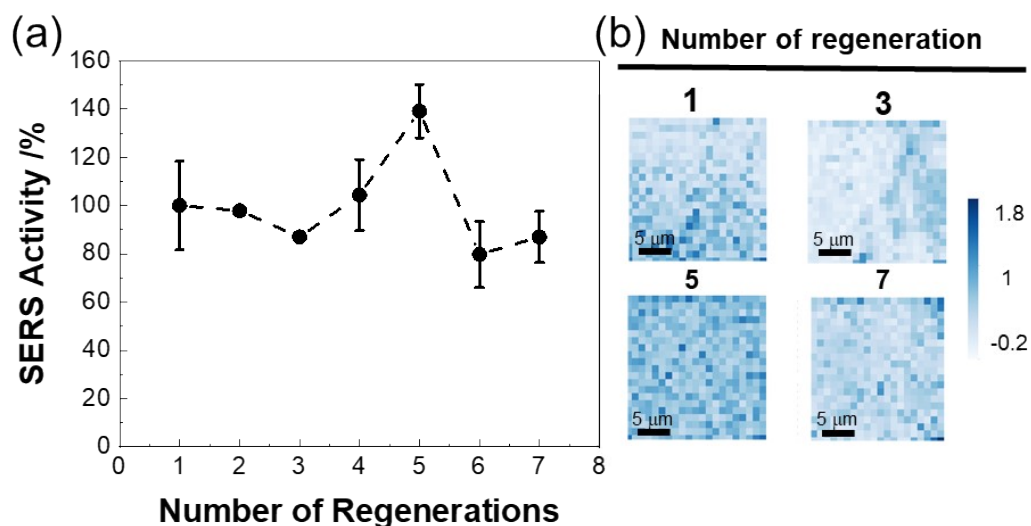

Figure S 13 - Capture platform reusability. (a) SERS activity of the biosensor along 7 regeneration cycles of the capture platform (b) Examples of pixelated SERS maps obtained for the indicated number of regeneration cycles. Error bars correspond to the standard deviation from three independent experiments.
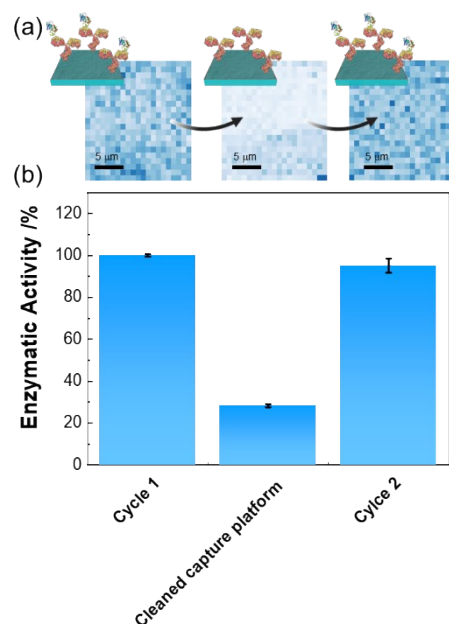

Figure S 14 - Capture platform reusability. (a) False-coloured SERS maps showing the SERS activity of the biosensor along two regeneration cycles of the capture platform as well as between the cycles. (b) Enzymatic activity of the biosensor along two regeneration cycles of the capture platform as well as between cycles. Error bars correspond to the standard deviation from three independent experiments.

12. Estimated cost of the proposed biosensor

Although an estimation for the cost is challenging without the knowledge of the facilities used for cellulose treatment, these reagents can be reused, significantly reducing the cost[29]. The cellulose market is a growing market and is expected to worth 1460 million US$ by the end of 2025[30]. This reflects the emergence of a new worldview that demands the adoption of sustainable concepts by making greater use of naturally abundant, renewable, and environmentally friendly raw materials, such as cellulose, that will play a key role in (bio)economy. The most expensive reagent used here is the antibody. Admitting a cost of around 400€ with an antibody at 90 mg/mL, the cost per capture platform (0.5 cm x 0.5 cm) would be 0.056€[31]. Due to the possibility of reusing the platform the prices decrease seven times. The cost of the SERS-immunotags will increase the price of the complete system by around 0.24€ due to the cost of the gold solution[32]. The proposed biosensor can then be regarded as a cost-efficient system.

References

1 M. J. Oliveira, M. P. de Almeida, D. Nunes, E. Fortunato, R. Martins, E. Pereira, H. J. Byrne, H. Águas and R. Franco, *Nanomaterials*, 2019, **9**, 1561.

2 I. Ojea-Jiménez, N. G. Bastús and V. Puntes, *J. Phys. Chem. C*, 2011, **115**, 15752–15757.

3 T. V. Tsoulos, L. Han, J. Weir, H. L. Xin and L. Fabris, *Nanoscale*, 2017, **9**, 3766–3773.

4 J. Langer, D. Jimenez de Aberasturi, J. Aizpurua, R. A. Alvarez-Puebla, B. Auguié, J. J. Baumberg, G. C. Bazan, S. E. J. Bell, A. Boisen, A. G. Brolo, J. Choo, D. Cialla-May, V. Deckert, L. Fabris, K. Faulds, F. J. García de Abajo, R. Goodacre, D. Graham, A. J. Haes, C. L. Haynes, C. Huck, T. Itoh, M. Käll, J. Kneipp, N. A. Kotov, H. Kuang, E. C. Le Ru, H. K. Lee, J.-F. Li, X. Y. Ling, S. A. Maier, T. Mayerhöfer, M. Moskovits, K. Murakoshi, J.-M. Nam, S. Nie, Y. Ozaki, I. Pastoriza-Santos, J. Perez-Juste, J. Popp, A. Pucci, S. Reich, B. Ren, G. C. Schatz, T. Shegai, S. Schlücker, L.-L. Tay, K. G. Thomas, Z.-Q. Tian, R. P. Van Duyne, T. Vo-Dinh, Y. Wang, K. A. Willets, C. Xu, H. Xu, Y. Xu, Y. S. Yamamoto, B. Zhao and L. M. Liz-Marzán, *ACS Nano*, 2020, **14**, 28–117.

5 H. de Puig, J. O. Tam, C.-W. Yen, L. Gehrke and K. Hamad-Schifferli, *J. Phys. Chem. C*, 2015, **119**, 17408–17415.

6 S. Barbosa, A. Agrawal, L. Rodríguez-Lorenzo, I. Pastoriza-Santos, R. A. Alvarez-Puebla, A. Kornowski, H. Weller and L. M. Liz-Marzán, *Langmuir*, 2010, **26**, 14943–14950.

7 C. L. Nehl, H. Liao and J. H. Hafner, *Nano Lett.*, 2006, **6**, 683–688.

8 V. Giannini, R. Rodríguez-Oliveros and J. A. Sánchez-Gil, *Plasmonics*, 2010, **5**, 99–104.

9 M. S. Jimenez, J. M. Luque-Alled, T. Gomez and J. R. Castillo, *Electrophoresis*, 2016, **37**, 1376–1383.

10 C. M. Silveira, R. Zumpano, M. Moreira, M. P. de Almeida, M. J. Oliveira, M. Bento, C. Montez, I. Paixão, R. Franco, E. Pereira and M. G. Almeida, *ChemElectroChem*, 2019, **6**, 4696–4703.

11 L. Piantanida, D. Naumenko and M. Lazzarino, *RSC Adv.*, 2014, **4**, 15281–15287.

12 M. A. S. Cavadas, M. P. Monopoli, C. S. e Cunha, M. Prudêncio, E. Pereira, I. Lynch, K. A. Dawson and R. Franco, *Part. Part. Syst. Charact.*, 2016, **33**, 906–915.

13 M. Peixoto de Almeida, P. Quaresma, S. Sousa, C. Couto, I. Gomes, L. Krippahl, R.

Franco and E. Pereira, *Phys. Chem. Chem. Phys.*, 2018, **20**, 16761–16769.

14   D. Bartczak and A. G. Kanaras, *Langmuir*, 2011, **27**, 10119–10123.

15   M. Rabe, D. Verdes and S. Seeger, *Adv. Colloid Interface Sci.*, 2011, **162**, 87–106.

16   M. J. E. Fischer, in *Life Sciences*, 2010, pp. 55–73.

17   S. Puertas, P. Batalla, M. Moros, E. Polo, P. del Pino, J. M. Guisán, V. Grazú and J. M. de la Fuente, *ACS Nano*, 2011, **5**, 4521–4528.

18   Thermo Fisher, *Chemical Reactivity of Crosslinkers and Modification Reagents*, 2012.

19   M. H. Jazayeri, H. Amani, A. A. Pourfatollah, H. Pazoki-Toroudi and B. Sedighimoghaddam, *Sens. Bio-Sensing Res.*, 2016, **9**, 17–22.

20   D. Bartczak, T. Sanchez-Elsner, F. Louafi, T. M. Millar and A. G. Kanaras, *Small*, 2011, **7**, 388–394.

21   G. T. Hermanson, *Bioconjugate Techniques: Third Edition*, Elsevier, London, Third., 2013.

22   J. Liu and Q. Peng, *Acta Biomater.*, 2017, **55**, 13–27.

23   A. Henriksen, D. J. Schuller, K. Meno, K. G. Welinder, A. T. Smith and M. Gajhede, *Biochemistry*, 1998, **37**, 8054–8060.

24   H. Orelma, I. Filpponen, L.-S. Johansson, M. Österberg, O. J. Rojas and J. Laine, *Biointerphases*, 2012, **7**, 61.

25   J. Łojewska, P. Miśkowiec, T. Łojewski and L. M. Proniewicz, *Polym. Degrad. Stab.*, 2005, **88**, 512–520.

26   C. K. Bayne and R. Kramer, *Technometrics*, 1999, 41, 173.

27   H. J. Byrne, P. Knief, M. E. Keating and F. Bonnier, *Chem. Soc. Rev.*, 2016, **45**, 1865–1878.

28   M. E. Keating, F. Bonnier and H. J. Byrne, *Analyst*, 2012, **137**, 5792.

29   A. Isogai, T. Saito and H. Fukuzumi, *Nanoscale*, 2011, **3**, 71–85.

30   I. B. Bwatanglang, Y. Musa and N. A. Yusof, *Sustain. Nanocellulose Nanohydrogels from Nat. Sources*, 2020, 65–79.

31   Anti-Horseradish Peroxidase antibody, https://www.antibodies-online.com/antibody/94386/anti-Horseradish+Peroxidase+HRP+antibody/, (accessed 21 July 2020).

32   Gold chloride solution, https://www.sigmaaldrich.com/PT/en/product/sigma/ht1004?context=product, (accessed 14 July 2021).